

Experimental and theoretical investigation of the co-occurrence of linear and circular dichroisms for oblique incidence of light on chiral sculptured thin films

Patrick D. McAtee and Akhlesh Lakhtakia

NanoMM—Nanoengineered Metamaterials Group, Department of Engineering Science and Mechanics, The Pennsylvania State University, University Park, Pennsylvania 16802, USA

Abstract

Theory shows that a slab of a dielectric structurally chiral material (DSCM) exhibits both linear and circular dichroisms because of its anisotropy and structural chirality, for normal as well as oblique incidence. This conclusion was confirmed by fabricating a chiral sculptured thin film and measuring the spectra of its reflectances and transmittances, both linear and circular. Signatures of the circular Bragg phenomenon are evident in the spectra of all reflectances, transmittances, absorptances, and dichroisms. Reversal of the structural handedness of a DSCM and rotation of the projection of the direction of propagation of the incident light clockwise instead of counterclockwise about the axis of helicoidal nonhomogeneity simultaneously changes the sign of circular dichroism but has no effect on linear dichroism.

1 Introduction

Free space is unirefringent as are isotropic dielectric materials that are the staple of undergraduate textbooks in the field of electromagnetics [1–3]. In a homogeneous unirefringent medium at a specific frequency, two plane waves of mutually orthogonal polarization states can propagate in a given direction, but both have the same wavenumber. In other words, their phase speeds and attenuation rates are identical but their polarization states are not.

Birefringent materials, often exemplified in undergraduate textbooks [4,5] by uniaxial dielectric materials such as calcite, are different from unirefringent mediums. Two plane waves of mutually orthogonal polarization states can propagate in a given direction in a homogeneous birefringent material at a specific frequency, but with different wavenumbers. Thus, their phase speeds, attenuation rates, and polarization states are different.

One of the two plane waves propagating in a particular direction in a homogeneous birefringent material will have a higher attenuation rate than the other, leading to the phenomenon of dichroism. If both plane waves are linearly polarized, as happens in uniaxial and biaxial dielectric materials lacking gyrotropy [6, Sec. 14.6.1], the phenomenon is qualified as *linear dichroism*. If both plane waves are circularly polarized, as happens in isotropic chiral materials [7,8], the phenomenon is qualified as *circular dichroism*.

Both uniaxiality and gyrotropy are present in a homogeneous dielectric material such as a magnetoplasma or a homogeneous magnetic material such as a ferrite. The relative permeability dyadic of a magnetoplasma is a scalar dyadic, whereas the relative permittivity dyadic can be stated in dyadic notation as [9, Chap. 7]

$$\underline{\underline{\varepsilon}}_r = \varepsilon_a \hat{\mathbf{u}}_z \hat{\mathbf{u}}_z + \varepsilon_b (\hat{\mathbf{u}}_x \hat{\mathbf{u}}_x + \hat{\mathbf{u}}_y \hat{\mathbf{u}}_y) + \varepsilon_g \times \underline{\underline{I}}, \quad (1)$$

where the relative permittivity scalars ε_a and ε_b together indicate uniaxiality; $\varepsilon_g \times \underline{\underline{I}}$ is the gyrotropic term with $\underline{\underline{I}}$ denoting the identity dyadic; and $\hat{\mathbf{u}}_x$, $\hat{\mathbf{u}}_y$, and $\hat{\mathbf{u}}_z$ are the three Cartesian unit vectors. The forms of the relative permeability and relative permittivity dyadics are reversed for a ferrite [9, Chap. 7]. Both linear dichroism and circular dichroism can simultaneously occur in such a material, but circular dichroism alone is observable when both plane waves propagate parallel to its sole optic axis (which is parallel to the

z axis). Circular dichroism can be induced in a unirefringent material by immersion in a strong magnetic field oriented parallel to the direction of light propagation [10,11].

Both linear dichroism and circular dichroism can simultaneously occur also in a non-gyrotropic dielectric material, provided it is structurally chiral [12–14]. This hypothesis underlaid a theoretical investigation of the spectral signatures of an axially excited slab of a dielectric structurally chiral material (DSCM) [15]. DSCMs are exemplified by chiral liquid crystals [16–18] and chiral sculptured thin films (CSTFs) [19–21]. The relative permittivity dyadic $\underline{\underline{\varepsilon}}_{\text{r}}$ of a DSCM is either uniaxial or biaxial and it varies helicoidally along a fixed axis (taken to be the z axis in this paper). Thus [14],

$$\underline{\underline{\varepsilon}}_{\text{r}}^{\text{DSCM}} = \underline{\underline{S}}_z(h, z, \Omega) \cdot S_y(\chi) \cdot [\varepsilon_a \hat{\mathbf{u}}_z \hat{\mathbf{u}}_z + \varepsilon_b \hat{\mathbf{u}}_x \hat{\mathbf{u}}_x + \varepsilon_c \hat{\mathbf{u}}_y \hat{\mathbf{u}}_y] \cdot \underline{\underline{S}}_y^{-1}(\chi) \cdot \underline{\underline{S}}_z^{-1}(h, z, \Omega), \quad (2)$$

where the relative permittivity scalars ε_a , ε_b , and ε_c indicate the local orthorhombicity of the DSCM;

$$\underline{\underline{S}}_y(\chi) = \hat{\mathbf{u}}_y \hat{\mathbf{u}}_y + (\hat{\mathbf{u}}_x \hat{\mathbf{u}}_x + \hat{\mathbf{u}}_z \hat{\mathbf{u}}_z) \cos \chi + (\hat{\mathbf{u}}_z \hat{\mathbf{u}}_x - \hat{\mathbf{u}}_x \hat{\mathbf{u}}_z) \sin \chi \quad (3)$$

contains $\chi \in (0 \text{ deg}, 90 \text{ deg}]$ is an angle of inclination with respect to the xy plane; and the rotation dyadic

$$\underline{\underline{S}}_z(h, z, \Omega) = \hat{\mathbf{u}}_z \hat{\mathbf{u}}_z + (\hat{\mathbf{u}}_x \hat{\mathbf{u}}_x + \hat{\mathbf{u}}_y \hat{\mathbf{u}}_y) \cos(\pi z / \Omega) + h (\hat{\mathbf{u}}_y \hat{\mathbf{u}}_x - \hat{\mathbf{u}}_x \hat{\mathbf{u}}_y) \sin(\pi z / \Omega) \quad (4)$$

contains $h \in \{-1, 1\}$ as the structural handedness parameter, where $h = -1$ for structural left-handedness and $h = 1$ for structural right-handedness, and 2Ω as the helicoidal period along the z axis. Gyrotropy has thus been replaced by helicoidal nonhomogeneity.

Theoretical investigation confirmed that when light is normally incident on a DSCM confined between the planes $z = 0$ and $z = L$, and the ratio $L/2\Omega$ is large enough, the DSCM must exhibit the circular Bragg phenomenon [14]. The signature of the circular Bragg phenomenon is twofold: (i) almost total reflection of the incident light of the co-handed circular-polarization state and (ii) very little reflection of the incident light of the cross-handed circular-polarization state. This signature occurs in a spectral regime called the circular Bragg regime.

The circular Bragg phenomenon was found to be accompanied by distinct features in the spectrums of both linear and circular dichroisms [15]. Linear dichroism pertains to the differential in the response to incident light of the s - and p -polarization states, whereas circular dichroism pertains to the differential in the response to incident light of the left- and right-circular polarization states.

Furthermore, a distinction emerged between true and apparent dichroisms. True dichroism is the differential in the absorbance whereas apparent dichroism is the differential in transmittance, with apparent dichroism requiring less effort to measure than true dichroism. Where true dichroism can only occur in a dissipative material, apparent dichroism can be exhibited even if dissipation is small enough to be ignored.

All data reported by Lakhtakia [15] were calculated by assuming $\varepsilon_a = \varepsilon_c$ and ε_b to be complex as well as frequency dependent. Later, similar data were published with respect to the porosity of a CSTF [22,23]. Very recently, nonzero values of true dichroisms of a zirconium-oxide CSTF were reported for oblique incidence [24,25], but the data must be incorrect because all three of ε_a , ε_b , and ε_c were assumed real and positive [26]; moreover, ε_a , ε_b , and ε_c were taken to be independent of frequency.

No experimental measurement of any of the four types of dichroisms—true linear $\mathcal{LD}_{\text{tru}}$, true circular $\mathcal{CD}_{\text{tru}}$, apparent linear $\mathcal{LD}_{\text{app}}$, and apparent circular $\mathcal{CD}_{\text{app}}$ —have ever been reported, which motivated us to experimentally investigate the co-exhibition of linear dichroism and circular dichroism by a DSCM. For this purpose, we fabricated a CSTF made of zinc selenide (ZnSe) using the serial-bideposition technique [27,28].

Spectral measurements of reflectance and transmittances were carried out for linearly as well as circularly polarized light obliquely incident of the CSTF over the 500-to-900-nm range of the free-space wavelength λ_0 [21, 28, 29]. We also performed a theoretical investigation in parallel.

This paper is organized as follows. Section 2.2.1 provides an overview of the formalism to define and calculate $\mathcal{LD}_{\text{tru}}$, $\mathcal{CD}_{\text{tru}}$, $\mathcal{LD}_{\text{app}}$, and $\mathcal{CD}_{\text{app}}$. An $\exp(-i\omega t)$ dependence on time t is explicit, with ω as the angular frequency and $i = \sqrt{-1}$. The free-space wavenumber is denoted by $k_0 = \omega\sqrt{\varepsilon_0\mu_0} = 2\pi/\lambda_0$, with ε_0 and μ_0 being the permittivity and permeability, respectively, of free space. Section 2.2.2 contains a description of the experimental procedures used for the fabrication as well as the morphological and optical characterization of the CSTF. Theoretical and experimental data for $\mathcal{LD}_{\text{tru}}$, $\mathcal{CD}_{\text{tru}}$, $\mathcal{LD}_{\text{app}}$, and $\mathcal{CD}_{\text{app}}$ are presented and discussed in Secs. 3 and 4, respectively.

2 Methods

2.1 Theory

2.1.1 Linear Reflectances and Transmittances

Suppose the region $0 < z < L$ is occupied by a CSTF of infinite transverse extent. The electric field phasor of the plane wave incident on the CSTF from the half space $z < 0$ is given by [20, 29]

$$\mathbf{E}_{\text{inc}}(x, y, z) = (a_s \hat{\mathbf{s}} + a_p \hat{\mathbf{p}}_+) \exp \{ ik_0 [(x \cos \psi + y \sin \psi) \times \sin \theta_{\text{inc}} + z \cos \theta_{\text{inc}}] \}, \quad z < 0, \quad (5)$$

where $\theta_{\text{inc}} \in [0 \text{ deg}, 90 \text{ deg})$ is the angle of incidence with respect to the z axis, $\psi \in [0 \text{ deg}, 360 \text{ deg})$ is the angle of incidence with respect to the x axis in the xy plane, a_s is the amplitude of the s -polarized component, and a_p is the amplitude of the p -polarized component. Here and hereafter, the unit vectors

$$\left. \begin{aligned} \hat{\mathbf{s}} &= -\hat{\mathbf{u}}_x \sin \psi + \hat{\mathbf{u}}_y \cos \psi \\ \hat{\mathbf{p}}_{\pm} &= \mp(\hat{\mathbf{u}}_x \cos \psi + \hat{\mathbf{u}}_y \sin \psi) \cos \theta_{\text{inc}} + \hat{\mathbf{u}}_z \sin \theta_{\text{inc}} \end{aligned} \right\} \quad (6)$$

delineate the orientations of the various field phasors.

The electric field phasor of the reflected plane wave is given by

$$\mathbf{E}_{\text{ref}}(x, y, z) = (r_s \hat{\mathbf{s}} + r_p \hat{\mathbf{p}}_-) \exp \{ ik_0 [(x \cos \psi + y \sin \psi) \sin \theta_{\text{inc}} - z \cos \theta_{\text{inc}}] \}, \quad z < 0, \quad (7)$$

and the electric field phasor of the transmitted plane wave by

$$\mathbf{E}_{\text{tr}}(x, y, z) = (t_s \hat{\mathbf{s}} + t_p \hat{\mathbf{p}}_+) \exp \{ ik_0 [(x \cos \psi + y \sin \psi) \times \sin \theta_{\text{inc}} - (z - L) \cos \theta_{\text{inc}}] \}, \quad z > L. \quad (8)$$

The reflection amplitudes r_s and r_p , as well as the transmission amplitudes t_s and t_p , have to be determined in terms of the incidence amplitudes a_s and a_p . The procedure is described in detail elsewhere [20, Chap. 9]. Thereafter, we can calculate the eight linear reflection and transmission coefficients appearing as the elements of the 2×2 matrices in the following relations [20, 29]:

$$\begin{bmatrix} r_s \\ r_p \end{bmatrix} = \begin{bmatrix} r_{ss} & r_{sp} \\ r_{ps} & r_{pp} \end{bmatrix} \begin{bmatrix} a_s \\ a_p \end{bmatrix}, \quad (9)$$

$$\begin{bmatrix} t_s \\ t_p \end{bmatrix} = \begin{bmatrix} t_{ss} & t_{sp} \\ t_{ps} & t_{pp} \end{bmatrix} \begin{bmatrix} a_s \\ a_p \end{bmatrix}. \quad (10)$$

Co-polarized coefficients have both subscripts identical, but cross-polarized coefficients do not. The square of the magnitude of a linear reflection or transmission coefficient is the corresponding linear reflectance or transmittance; thus, $R_{\text{sp}} = |r_{\text{sp}}|^2$ is the linear reflectance corresponding to the linear reflection coefficient r_{sp} , and so on.

2.1.2 Circular Reflectances and Transmittances

The procedure to determine the circular reflectances and transmittances is very similar [20, Chap. 9]. Let a_{L} be the amplitude of the left-circularly polarized component and a_{R} be the amplitude of the right-circularly polarized component of the incident plane wave. Then,

$$\left. \begin{aligned} a_{\text{L}} &= -\frac{1}{\sqrt{2}}(ia_{\text{s}} + a_{\text{p}}) \\ a_{\text{R}} &= \frac{1}{\sqrt{2}}(ia_{\text{s}} - a_{\text{p}}) \end{aligned} \right\}. \quad (11)$$

With r_{L} , r_{R} , t_{L} , and t_{R} denoting the circularly polarized components of the reflected and transmitted plane waves, we have

$$\left. \begin{aligned} r_{\text{L}} &= \frac{1}{\sqrt{2}}(ir_{\text{s}} + r_{\text{p}}) \\ r_{\text{R}} &= -\frac{1}{\sqrt{2}}(ir_{\text{s}} - r_{\text{p}}) \end{aligned} \right\}. \quad (12)$$

and

$$\left. \begin{aligned} t_{\text{L}} &= -\frac{1}{\sqrt{2}}(it_{\text{s}} + t_{\text{p}}) \\ t_{\text{R}} &= \frac{1}{\sqrt{2}}(it_{\text{s}} - t_{\text{p}}) \end{aligned} \right\}. \quad (13)$$

Accordingly, eight circular reflection and transmission coefficients can be defined as the elements of the 2×2 matrices in the following relations [20]:

$$\begin{bmatrix} r_{\text{L}} \\ r_{\text{R}} \end{bmatrix} = \begin{bmatrix} r_{\text{LL}} & r_{\text{LR}} \\ r_{\text{RL}} & r_{\text{RR}} \end{bmatrix} \begin{bmatrix} a_{\text{L}} \\ a_{\text{R}} \end{bmatrix}, \quad (14)$$

$$\begin{bmatrix} t_{\text{L}} \\ t_{\text{R}} \end{bmatrix} = \begin{bmatrix} t_{\text{LL}} & t_{\text{LR}} \\ t_{\text{RL}} & t_{\text{RR}} \end{bmatrix} \begin{bmatrix} a_{\text{L}} \\ a_{\text{R}} \end{bmatrix}. \quad (15)$$

The square of the magnitude of a circular reflection or transmission coefficient is the corresponding circular reflectance or transmittance; thus, $R_{\text{LR}} = |r_{\text{LR}}|^2$ is the circular reflectance corresponding to the circular reflection coefficient r_{LR} , and so on.

2.1.3 True Dichroisms

True dichroisms quantify differential absorption. Hence, we define the linear absorptances

$$\left. \begin{aligned} A_{\text{s}} &= 1 - (R_{\text{s}} + T_{\text{s}}) \in [0, 1] \\ A_{\text{p}} &= 1 - (R_{\text{p}} + T_{\text{p}}) \in [0, 1] \end{aligned} \right\} \quad (16)$$

and the circular absorptances

$$\left. \begin{aligned} A_{\text{L}} &= 1 - (R_{\text{L}} + T_{\text{L}}) \in [0, 1] \\ A_{\text{R}} &= 1 - (R_{\text{R}} + T_{\text{R}}) \in [0, 1] \end{aligned} \right\}, \quad (17)$$

where the total reflectances

$$\left. \begin{aligned} R_s &= R_{ss} + R_{ps} \in [0, 1] \\ R_p &= R_{pp} + R_{sp} \in [0, 1] \\ R_L &= R_{LL} + R_{RL} \in [0, 1] \\ R_R &= R_{RR} + R_{LR} \in [0, 1] \end{aligned} \right\} \quad (18)$$

and the total transmittances

$$\left. \begin{aligned} T_s &= T_{ss} + T_{ps} \in [0, 1] \\ T_p &= T_{pp} + T_{sp} \in [0, 1] \\ T_L &= T_{LL} + T_{RL} \in [0, 1] \\ T_R &= T_{RR} + T_{LR} \in [0, 1] \end{aligned} \right\} . \quad (19)$$

The true linear dichroism is then given by

$$\mathcal{LD}_{\text{tru}} = \sqrt{A_s} - \sqrt{A_p} \quad (20)$$

and the true circular dichroism by

$$\mathcal{CD}_{\text{tru}} = \sqrt{A_R} - \sqrt{A_L} . \quad (21)$$

2.1.4 Apparent Dichroisms

Apparent dichroisms quantify differential transmission. Hence, the apparent linear dichroism is given by [20, Chap. 9]

$$\mathcal{LD}_{\text{app}} = \sqrt{T_s} - \sqrt{T_p} \quad (22)$$

and the apparent circular dichroism by [20, Chap. 9]

$$\mathcal{CD}_{\text{app}} = \sqrt{T_R} - \sqrt{T_L} . \quad (23)$$

2.1.5 Calculation Parameters

All calculations were made by assuming single-resonance Lorentzian dependences on λ_0 for ε_a , ε_b , and ε_c ; thus [30],

$$\varepsilon_{a,b,c}(\lambda_0) = 1 + \frac{p_{a,b,c}}{1 + (1/N_{a,b,c} - i\lambda_{a,b,c}/\lambda_0)^2} . \quad (24)$$

The oscillator strengths are determined by the values of $p_{a,b,c}$, $\lambda_{a,b,c}(1 + N_{a,b,c}^{-2})^{-1/2}$ are the resonance wavelengths, and $\lambda_{a,b,c}/N_{a,b,c}$ are the resonance linewidths. The larger the values of $N_{a,b,c}$, the narrower are the absorption bands.

The parameters used for theoretical data reported here are as follows: $p_a = 2.3$, $p_b = 3.0$, $p_c = 2.2$, $\lambda_a = \lambda_c = 260$ nm, $\lambda_b = 270$ nm, and $N_a = N_b = N_c = 130$. Furthermore, $h = 1$, $\chi = 37$ deg, $\Omega = 150$ nm, $L = 20\Omega$, and $\psi = 0$ deg.

2.2 Experiments

2.2.1 Fabrication of CSTF

The CSTF for this project was fabricated using thermal evaporation implemented inside a low-pressure chamber [31] from Torr International (New Windsor, New York). It contains a quartz crystal monitor

calibrated to measure the growing thin-film's thickness, a receptacle to hold the material to be evaporated to generate a collimated vapor flux, electrodes to resistively heat the receptacle, and a substrate holder positioned about 15 cm directly above the receptacle. As the chamber was customized to grow CSTFs [21], it contains two stepper motors to control the rotation of the substrate holder about two mutually orthogonal axes, one passing normally through the substrate holder to serve as the z axis, and the second serving as the y axis in the substrate (xy) plane.

The motors were programmed such that $\Omega = 150$ nm. The angle of the collimated vapor flux with respect to the substrate plane set at $\chi_v = 20$ deg corresponding to $\chi = 37$ deg, as determined experimentally elsewhere [28]. 99.995 % pure ZnSe (Alfa Aesar, Ward Hill, Massachusetts) was the material of choice due to its high bulk index of refraction and low absorption in the visible spectral regime [32,33] as well as its ease of evaporation. The manufacturer supplied ZnSe lumps that were crushed into a fine powder. A respirator was worn to avoid the toxic effects of ZnSe on the respiratory system [34].

Approximately 4.2 g of ZnSe powder was packed into a tungsten boat (S22-.005W, R. D. Mathis, Long Beach, California) that served as the receptacle. Then the substrate was further cleaned in an ethanol bath using an ultrasonicator for 10 min on each side. After removal from the bath, the substrate was immediately dried with pressurized nitrogen gas. The substrate was carefully secured to the substrate holder using Kapton tape (S-14532, Uline, Pleasant Prairie, Wisconsin), and a shutter was interposed between the receptacle and the substrate holder. By the side of the glass substrate, a silicon wafer was positioned in order to grow a sample for imaging on a scanning electron microscope.

The chamber was pumped down to 1 μ Torr. The current through the receptacle was then slowly increased to ~ 100 A, and the shutter was rotated to allow a collimated portion of the ZnSe vapor flux to reach the substrate and the wafer. The deposition rate as read through the quartz crystal monitor was manually maintained equal to 0.4 ± 0.02 nm s $^{-1}$. After the deposition was completed, the shutter was rotated to prevent further deposition, the current was brought back to 0 A, the chamber was allowed to cool down for 60 min, and was then exposed to the atmosphere. The CSTF was grown in two stages, each depositing $5 \times 2\Omega$. Thus, the total thickness was $L = 20\Omega$.

The CSTF was grown using the serial-bideposition technique described as follows [27]. A subdeposit is made for time τ_1 , followed by a rapid rotation about the z axis by angle Ψ in time τ_a , followed by another subdeposit for time τ_1 , followed by a rapid rotation about the z axis by angle $\Psi + \delta$ in time $\tau_b > \tau_a$, and so on. Therefore, the total time to deposit one pair of subdeposits is given by $\tau_{\text{sdp}} = 2\tau_1 + \tau_a + \tau_b$. If N_{sdp} is the number of subdeposit-pairs per period, the total deposition time for one period is given by $\tau_{\text{per}} = N_{\text{sdp}}\tau_{\text{sdp}}$. We fixed $\Psi = 180$ deg, $\delta = 3$ deg, $\tau_a = 0.406$ s, $\tau_b = 0.413$ s, and $\tau_{\text{per}} = 750$ s. Accordingly, $N_{\text{sdp}} = 360/3 = 120$, $\tau_{\text{sdp}} = 750/120 = 6.25$ s, and $\tau_1 = 2.7155$ s.

2.2.2 Morphological Characterization

The cross-sectional morphology of the CSTF sample was determined using an FEI Nova NanoSEM 630 (FEI, Hillsboro, Oregon) field-emission scanning electron microscope. To get a clear image of morphology away from any edge-growth effects, each sample was cleaved using the freeze-fracture technique [35]. The sample was sputtered with iridium using a Quorum Emitech K575X (Quorum Technologies, Ashford, Kent, United Kingdom) sputter coater before imaging.

2.2.3 Optical Characterization

All transmittance and reflectance measurements were made within 24 h after fabrication. The sample was kept in a desiccator up until the time of optical characterization in order to prevent degradation due to moisture adsorption. The experimental setups for reflection and transmission measurements for $\lambda_0 \in [500 \text{ nm}, 900 \text{ nm}]$ are described in detail elsewhere [28, 29]. All measurements were taken in a dark room to avoid noise from external sources, and we ensured that ψ was the same for all measurements.

Briefly, light from a halogen source (HL-2000, Ocean Optics, Dunedin, Florida) was passed through a fiber-optic cable and then through a linear polarizer (GT10, ThorLabs, Newton, New Jersey); it was either reflected from or transmitted through the sample to be characterized and was then passed through a second linear polarizer (GT10, ThorLabs) and a fiber-optic cable to a CCD spectrometer (HRS-BD1-025, Mightex Systems, Pleasanton, California) [29]. The linear transmittances T_{ss} , T_{ps} , T_{sp} , and T_{pp} were measured for $\theta_{\text{inc}} \in [0 \text{ deg}, 70 \text{ deg}]$, and the linear reflectances R_{ss} , R_{ps} , R_{sp} , and R_{pp} for $\theta_{\text{inc}} \in [10 \text{ deg}, 70 \text{ deg}]$.

For measurements of the circular reflectances and transmittances, a Fresnel rhomb (LMR1, ThorLabs) was introduced directly after the first linear polarizer and another Fresnel rhomb directly before the second linear polarizer [28]. The circular transmittances T_{LL} , T_{RL} , T_{LR} , and T_{RR} were measured for $\theta_{\text{inc}} \in [0 \text{ deg}, 70 \text{ deg}]$, and the linear reflectances R_{LL} , R_{RL} , R_{LR} , and R_{RR} for $\theta_{\text{inc}} \in [10 \text{ deg}, 70 \text{ deg}]$.

3 Theoretical Results

3.1 Circular Reflectances and Transmittances

As DSCMs exhibit the circular Bragg phenomenon, their circular reflectances and transmittances for normal incidence have been of major interest for both theorists and experimentalists for several decades [14]. Theoretical results for oblique incidence have also been published [36–42], but experimental data for oblique incidence are rare and incomprehensive [36, 42–47]. Although spectrums of the circular reflectances and transmittances over wide ranges of both λ_0 and θ_{inc} have recently been published [21, 48], we provide calculated values of R_L , R_R , T_L , and T_R as functions of λ_0 and θ_{inc} in Fig. 1 both for completeness as well as to contextualize novel results.

The circular Bragg phenomenon is manifest in Fig. 1 as a high ridge in the graph of R_R and a correspondingly deep trough in the graph of T_R . For $\theta_{\text{inc}} \in \{10 \text{ deg}, 30 \text{ deg}, 70 \text{ deg}\}$, values of the center wavelength of the circular Bragg regime were estimated as $\lambda_0^{\text{Br}} \in \{599 \text{ nm}, 584 \text{ nm}, 549 \text{ nm}\}$ from both of these graphs. Thus, the circular Bragg regime blueshifts as the incidence becomes more oblique. A trough in the graph of R_L and a ridge in the graph of T_L are also evident.

All of the foregoing features arose because we set $h = 1$ for calculations. As a result, the CSTF was chosen to be structurally right handed so that incident right-circularly polarized light must be reflected much more than incident left-circularly polarized light in the circular Bragg regime. If we had set $h = -1$, the CSTF would have been structurally left handed so that incident left-circularly polarized light would have been reflected much more than incident right-circularly polarized light.

3.2 True and Apparent Circular Dichroisms

Figure 1 also shows graphs of A_L and A_R as functions of λ_0 and θ_{inc} . The circular Bragg phenomenon is faintly evident as a ridge in the graph of A_L and clearly as a trough in the graph of A_R . Therefore, in the

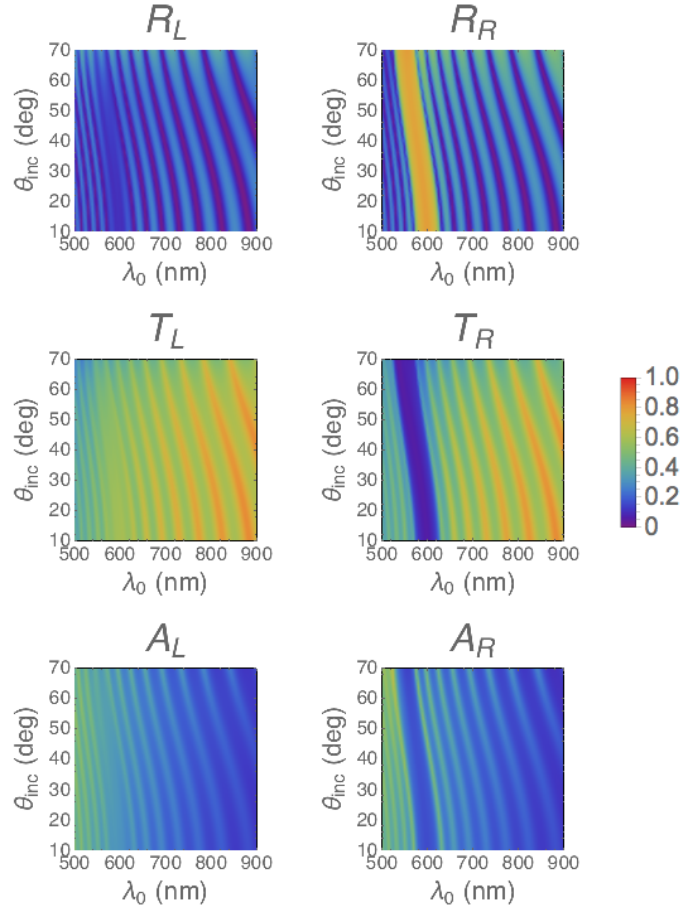


Figure 1: R_L , R_R , T_L , T_R , A_L , and A_R calculated as functions of λ_0 and θ_{inc} for $h = 1$ and $\psi = 0$ deg.

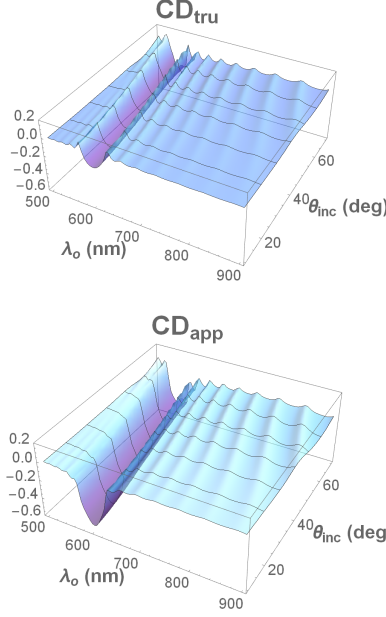


Figure 2: $\mathcal{CD}_{\text{tru}}$ and $\mathcal{CD}_{\text{app}}$ calculated as functions of λ_0 and θ_{inc} for $h = 1$ and $\psi = 0$ deg.

circular Bragg regime, $A_L \neq A_R$ so that $\mathcal{CD}_{\text{tru}} \neq 0$; furthermore, $\mathcal{CD}_{\text{app}} \neq 0$ because $T_L \neq T_R$ in Fig. 1.

Graphs of $\mathcal{CD}_{\text{tru}}$ and $\mathcal{CD}_{\text{app}}$ as functions of λ_0 and θ_{inc} are provided in Fig. 2. Both graphs have troughs coincident with the manifestation of the circular Bragg phenomenon in Fig. 1. For $\theta_{\text{inc}} \in \{10 \text{ deg}, 30 \text{ deg}, 70 \text{ deg}\}$, values of the center wavelength of the circular Bragg regime were estimated as $\lambda_0^{\text{Br}} \in \{598 \text{ nm}, 584 \text{ nm}, 546 \text{ nm}\}$ from both graphs in Fig. 2. These estimates are just 1.0 nm, 0.0 nm, and 3.0 nm different from the estimates drawn from Fig. 1.

Given the definition of $\mathcal{CD}_{\text{tru}}$ in Eq. (21), we expect that $\mathcal{CD}_{\text{tru}} < 0$ in the circular Bragg regime because $\{h = 1, L \gg 2\Omega\} \implies A_R < A_L$. Likewise, in view of its definition in Eq. (23), we expect that $\mathcal{CD}_{\text{app}} < 0$ in the circular Bragg regime because $\{h = 1, L \gg 2\Omega\} \implies T_R < T_L$ if the CSTF is not strongly dissipative. Both of these expectations are borne out by the graphs in Fig. 2, especially in the central portion of the circular Bragg regime.

Let us also note a significant symmetry evinced by circular reflectances and transmittances. If the replacement $\{h \rightarrow -h, \psi \rightarrow -\psi\}$ is made, then the interchanges $\{R_{\text{RR}} \leftrightarrow R_{\text{LL}}, R_{\text{LR}} \leftrightarrow R_{\text{RL}}, T_{\text{RR}} \leftrightarrow T_{\text{LL}}, T_{\text{LR}} \leftrightarrow T_{\text{RL}}\}$ follow. Accordingly, the replacement $\{h \rightarrow -h, \psi \rightarrow -\psi\}$ implies that $\{\mathcal{CD}_{\text{tru}} \rightarrow -\mathcal{CD}_{\text{tru}}, \mathcal{CD}_{\text{app}} \rightarrow -\mathcal{CD}_{\text{app}}\}$. For arbitrary values of ψ , the replacement $h \rightarrow -h$ affects both $\mathcal{CD}_{\text{tru}}$ and $\mathcal{CD}_{\text{app}}$.

3.3 Linear Reflectances and Transmittances

The linear reflectances and transmittances of DSCMs have been investigated very little [15, 20], for which reason we provide calculated values of R_s , R_p , T_s , and T_p in relation to both λ_0 and θ_{inc} in Fig. 3. In these graphs, the circular Bragg phenomenon has a split signature: a ridge and a trough side by side in the graphs of both R_s and R_p , and a trough and a ridge side by side in the graphs of both T_s and T_p . The blueshift of the circular Bragg phenomenon with oblique incidence is also captured in these graphs.

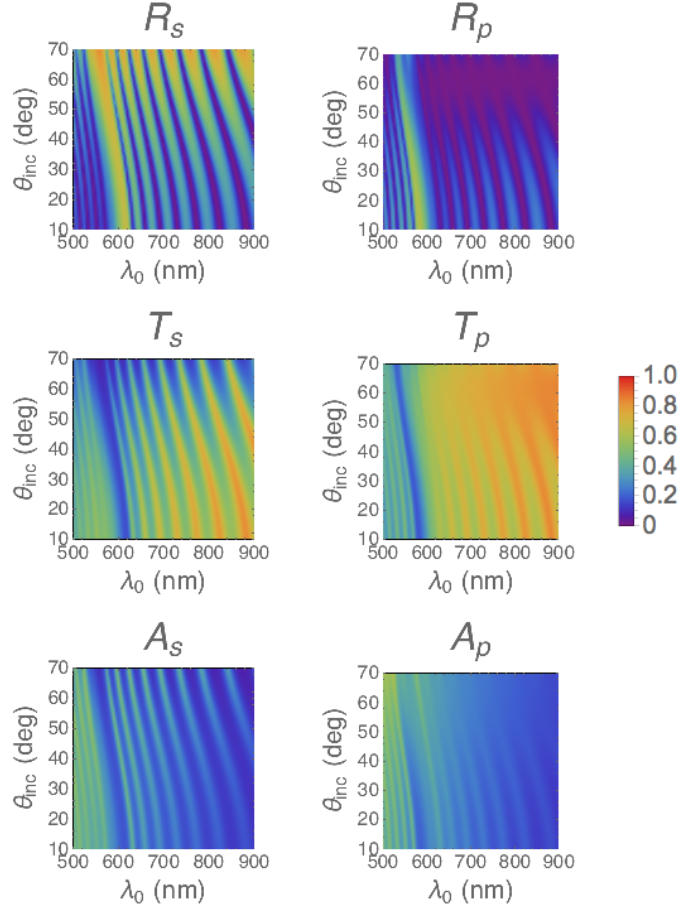


Figure 3: R_s , R_p , T_s , T_p , A_s , and A_p calculated as functions of λ_0 and θ_{inc} for $h = \pm 1$ and $\psi = 0$ deg.

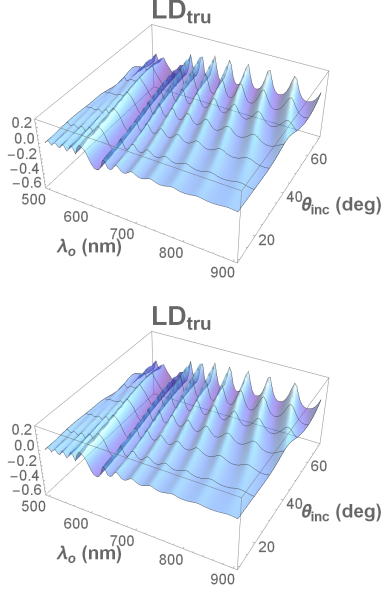


Figure 4: $\mathcal{LD}_{\text{tru}}$ and $\mathcal{LD}_{\text{app}}$ calculated as functions of λ_0 and θ_{inc} for $h = \pm 1$ and $\psi = 0$ deg.

3.4 True and Apparent Linear Dichroisms

In general, T_s and T_p are unequal in Fig. 3 as also are A_s and A_p . Therefore, $\mathcal{LD}_{\text{tru}} \neq 0$ and $\mathcal{LD}_{\text{app}} \neq 0$, as depicted in Fig. 4. The graphs of $\mathcal{LD}_{\text{tru}}$ and $\mathcal{LD}_{\text{app}}$ as functions of λ_0 and θ_{inc} clearly trace out the circular Bragg phenomenon in the form of a ridge by the side of a trough, both of which blueshift as θ_{inc} increases.

A change in the structural handedness does not affect the graphs in Fig. 3 because $\psi = 0$ deg. Indeed, all eight linear reflectances and transmittances remain unaffected by the replacement $\{h \rightarrow -h, \psi \rightarrow -\psi\}$. Hence, that replacement affects neither $\mathcal{LD}_{\text{tru}}$ nor $\mathcal{LD}_{\text{app}}$. For arbitrary values of ψ , the replacement $h \rightarrow -h$ affects both $\mathcal{LD}_{\text{tru}}$ and $\mathcal{LD}_{\text{app}}$.

4 Experimental Results

4.1 Morphology

The scanning-electron micrograph in Fig. 5 shows that the overall thickness L of the ZnSe CSTF is $3.11 \mu\text{m}$; thus, the period 2Ω is equal to 311 nm. This is just 3.7% more than the targeted value of 300 nm.

4.2 Circular Reflectances, Transmittances, and Dichroisms

Figure 6 provides measured values of R_L , R_R , T_L , T_R , A_L , and A_R as functions of λ_0 and θ_{inc} . Due to mechanical limitations of the optical apparatus, reflectances could only be measured for $\theta_{\text{inc}} \geq 10$ deg, which limited the absorbance data to $\theta_{\text{inc}} \in \{10 \text{ deg}, 70 \text{ deg}\}$.

The circular Bragg phenomenon is manifest in Fig. 6 as a high ridge in the graph of R_R and a correspondingly deep trough in the graph of T_R . For $\theta_{\text{inc}} \in \{10 \text{ deg}, 30 \text{ deg}, 70 \text{ deg}\}$, values of the center wavelength of the circular Bragg regime were estimated as $\lambda_0^{\text{Br}} \in \{596.8 \text{ nm}, 586.1 \text{ nm}, 551.9 \text{ nm}\}$ from both of these

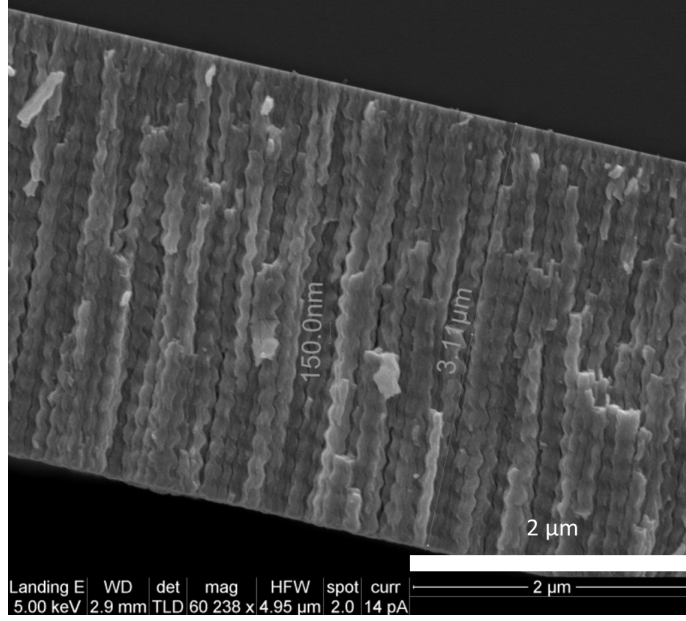


Figure 5: Cross-sectional scanning-electron micrograph of the ZnSe CSTF fabricated for this research.

graphs. Also, the circular Bragg phenomenon is clearly evident as a trough in the graphs of R_L and A_R and faintly as a ridge in the graphs of T_L and A_L . Also, the circular Bragg regime blueshifts as the incidence becomes more oblique. All of these features are in accord with the data calculated for Fig. 1.

Graphs of $\mathcal{CD}_{\text{tru}}$ and $\mathcal{CD}_{\text{app}}$ measured as functions of λ_0 and θ_{inc} are provided in Fig. 7. The trough in the graph of $\mathcal{CD}_{\text{tru}}$ indicative of the circular Bragg regime is less deep, of narrower bandwidth, and redshifted in comparison to its counterpart in the graph of $\mathcal{CD}_{\text{app}}$. These features are somewhat different than those in the theoretical graphs of Fig. 2, thereby indicating that the single-resonance Lorentzian dependences of $\varepsilon_{a,b,c}$ on λ_0 require some modification [21].

4.3 Linear Reflectances, Transmittances, and Dichroisms

Measured values of R_s , R_p , T_s , and T_p are provided in relation to λ_0 and θ_{inc} in Fig. 8. In all four graphs, the circular Bragg phenomenon is clearly evident along with its blueshift with oblique incidence.

From the data for A_s and A_p also depicted in Fig. 8, we computed both $\mathcal{LD}_{\text{tru}}$ and $\mathcal{LD}_{\text{app}}$ as functions of λ_0 and θ_{inc} for presentation in Fig. 9. The circular Bragg phenomenon is manifest in all four graphs. As the value of ψ could not be known, a more robust comparison with Figs. 3 and 4 is not possible.

5 Concluding Remarks

We have provided both theoretical and experimental evidence for the simultaneous exhibition of linear and circular dichroisms by a dielectric structural chiral material. Whereas both $\mathcal{CD}_{\text{tru}}$ and $\mathcal{LD}_{\text{tru}}$ arise from dissipation in the DSCM, $\mathcal{CD}_{\text{app}}$ and $\mathcal{LD}_{\text{app}}$ can be exhibited even if dissipation was weak enough to be ignored. The co-occurrence of both linear and circular dichroisms can only be attributed to the structural

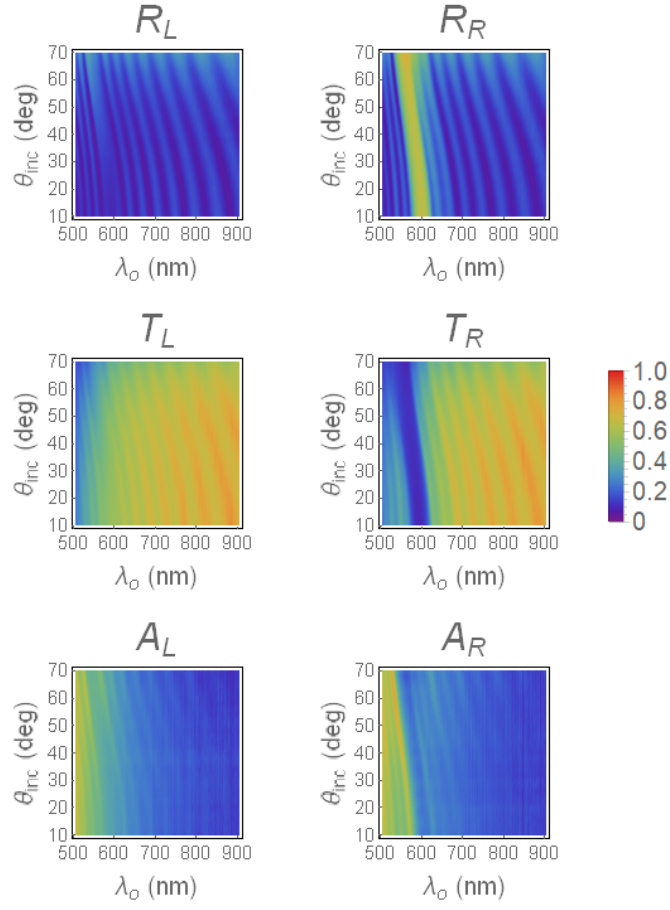


Figure 6: R_L , R_R , T_L , T_R , A_L , and A_R measured as functions of λ_o and θ_{inc} for $h = 1$.

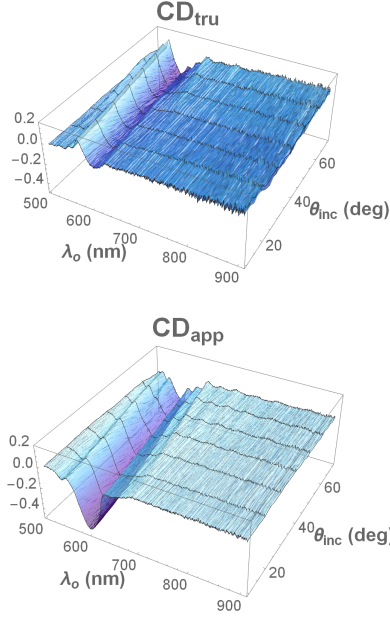


Figure 7: $\mathcal{CD}_{\text{tru}}$ and $\mathcal{CD}_{\text{app}}$ measured as functions of λ_0 and θ_{inc} for $h = 1$ and $\psi = 0$ deg.

chirality of a DSCM, gyrotropy being absent therein.

Our investigation covered a wide enough spectral regime to encompass the exhibition of the circular Bragg phenomenon by the chosen DSCM. This phenomenon is manifested not only in the graphs of circular reflectances and transmittances but also in the graphs of linear reflectances and transmittances. Furthermore, the circular Bragg phenomenon is manifested in the spectrums of $\mathcal{CD}_{\text{tru}}$, $\mathcal{LD}_{\text{tru}}$, $\mathcal{CD}_{\text{app}}$ and $\mathcal{LD}_{\text{app}}$. The blueshift of the circular Bragg phenomenon with increasingly oblique incidence was also captured in the spectrums of linear reflectances and transmittances as well as in the spectrums of circular and linear dichroisms.

We found from theory that reversing the structural handedness (i.e., $h \rightarrow -h$) of a DSCM and rotating the projection of the direction of propagation of the incident light clockwise instead of counterclockwise (i.e., $\psi \rightarrow -\psi$) about the axis of helicoidal nonhomogeneity (z axis) simultaneously changes the signs of both $\mathcal{CD}_{\text{tru}}$ and $\mathcal{CD}_{\text{app}}$. However, the simultaneous reversals have no effect on both $\mathcal{LD}_{\text{tru}}$ and $\mathcal{LD}_{\text{app}}$.

Before concluding, we must compare our findings with those for quartz. Quartz is a homogeneous material with a uniaxial permittivity dyadic and can display linear dichroism [49]. However, even in the early 1800s, natural optical activity was observed when both plane waves propagate parallel to the sole optic axis of the material, as was remarked upon by Condon [50]. As has been inferred only very recently by experimentation [52], quartz has to be characterized as a homogeneous bianisotropic material [51], whose permittivity and both magnetoelectric dyadics are uniaxial and whose permeability dyadic is scalar. In contrast, the DSCMs considered in our work are purely dielectric materials without gyrotropy but are nonhomogeneous along a fixed direction [17–21].

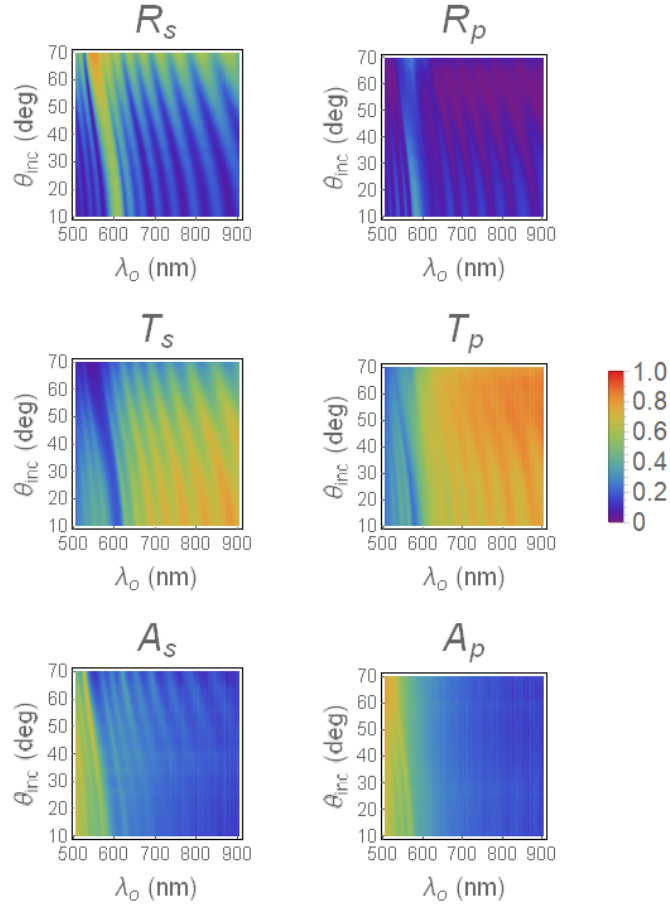


Figure 8: R_s , R_p , T_s , T_p , A_s , and A_p measured as functions of λ_o and θ_{inc} for $h = 1$ and $\psi = 0$ deg.

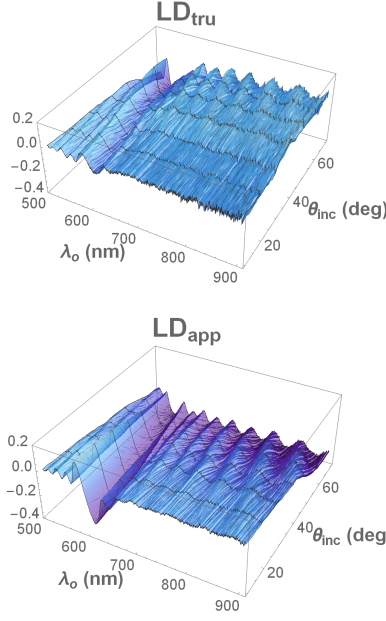


Figure 9: $\mathcal{LD}_{\text{tru}}$ and $\mathcal{LD}_{\text{app}}$ measured as functions of λ_o and θ_{inc} for $h = 1$ and $\psi = 0$ deg.

References

- [1] R. F. Harrington, *Time-Harmonic Electromagnetic Fields* (IEEE Press, 2001).
- [2] B. Guru and H. Hiziroğlu, *Electromagnetic Field Theory Fundamentals*, 2nd edn. (Cambridge Univ. Press, 2004).
- [3] M. F. Iskander, *Electromagnetic Fields and Waves*, 2nd edn. (Waveland Press, 2013).
- [4] A. K. Ghatak and K. Thyagarajan, *Optical Electronics* (Cambridge Univ. Press, 1989).
- [5] E. Hecht, *Optics*, 5th edn. (Pearson, 2017).
- [6] M. Born and E. Wolf, *Principles of Optics*, 6th edn. (Pergamon, 1987).
- [7] E. Charney, *The Molecular Basis of Optical Activity* (Krieger, 1985).
- [8] A. Lakhtakia, *Beltrami Fields in Chiral Media* (World Scientific, 1994).
- [9] H. C. Chen, *Theory of Electromagnetic Waves* (McGraw-Hill, 1983).
- [10] D. Caldwell, J. M. Thorne, and H. Eyring, "Magnetic circular dichroism," *Annu. Rev. Phys. Chem.* **22** 259–278 (1971).
- [11] P. J. Stephens, "Magnetic circular dichroism," *Annu. Rev. Phys. Chem.* **25** 201–232 (1974).
- [12] E. Reusch, "Untersuchung über Glimmercombinationen," *Ann. Phys. Chem. Lpz.* **138**, 628–638 (1869).

- [13] J. C. Bose, “On the rotation of plane of polarisation of electric waves by a twisted structure,” *Proc. R. Soc. Lond.* **63**, 146–152 (1898).
- [14] M. Faryad and A. Lakhtakia, “The circular Bragg phenomenon,” *Adv. Opt. Photon.* **6**, 225–292 (2014).
- [15] A. Lakhtakia, “Spectral signatures of axially excited slabs of dielectric thin-film helicoidal bianisotropic mediums,” *Eur. Phys. J. AP* **8**, 129–137 (1999).
- [16] S. Chandrasekhar, *Liquid Crystals*, 2nd edn. (Cambridge Univ. Press, 1992).
- [17] P. G. de Gennes and J. Prost, *The Physics of Liquid Crystals*, 2nd edn. (Clarendon Press, 1993).
- [18] R. Nityananda, U. D. Kini, S. Chandrasekhar, and K. A. Suresh, “Anomalous transmission (Borrmann effect) in absorbing cholesteric liquid crystals,” in *Proceedings of the International Liquid Crystal Conference*, Bangalore, December 3–8, 1973, *Pramana Suppl.* **1**, 325–340 (1975).
- [19] N. O. Young and J. Kowal, “Optically active fluorite films,” *Nature* **183**, 104–105 (1959).
- [20] A. Lakhtakia and R. Messier, *Sculptured Thin Films: Nanoengineered Morphology and Optics*, (SPIE Press, 2005).
- [21] S. Erten, A. Lakhtakia, and G. D. Barber, “Experimental investigation of circular Bragg phenomenon for oblique incidence,” *J. Opt. Soc. Am. A* **32**, 764–770 (2015).
- [22] J. A. Sherwin and A. Lakhtakia, “Nominal model for structure-property relations of chiral dielectric sculptured thin films,” *Math. Comput. Model.* **34**, 1499–1514 (2001).
- [23] J. A. Sherwin and A. Lakhtakia, “Errata to: Nominal model for structure-property relations of chiral dielectric sculptured thin films,” *Math. Comput. Model.* **35**, 1355–1363 (2002).
- [24] Z. Muhammad, F. Wali, and L. Song, “Co-occurrence of linear and circular dichroism in chiral sculptured ZrO_2 thin films,” *Opt. Mater.* **75**, 319–324 (2018).
- [25] Z. Muhammad, F. Wali, and L. Song, “Corrigendum to: Co-occurrence of linear and circular dichroism in chiral sculptured ZrO_2 thin films,” *Opt. Mater.* **75**, xxx (2018); <https://doi.org/10.1016/j.optmat.2017.12.050>.
- [26] I. Hodgkinson, Q. h. Wu, and J. Hazel, “Empirical equations for the principal refractive indices and column angle of obliquely deposited films of tantalum oxide, titanium oxide, and zirconium oxide,” *Appl. Opt.* **37**, 2653–2659 (1998).
- [27] I. Hodgkinson, Q. h. Wu, B. Knight, A. Lakhtakia, and K. Robbie, “Vacuum deposition of chiral sculptured thin films with high optical activity,” *Appl. Opt.* **39**, 642–649 (2000).
- [28] P. D. McAtee and A. Lakhtakia, “Reflection and transmission of obliquely incident light by chiral sculptured thin films fabricated using asymmetric serial-bideposition technique,” *J. Nanophoton.* **11**, 043502 (2017).
- [29] V. Vepachedu, P. D. McAtee, and A. Lakhtakia, “Nonexhibition of Bragg phenomenon by chevronic sculptured thin films: experiment and theory,” *J. Nanophoton.* **11**, 036018 (2017).

- [30] C. Kittel, *Introduction to Solid State Physics* (Wiley Eastern, 1974).
- [31] S. E. Swiontek and A. Lakhtakia, “Vacuum-metal-deposition and columnar-thin-film techniques implemented in the same apparatus,” *Mater. Lett.* **142**, 291–293 (2015).
- [32] ThorLabs, “Zinc selenide (ZnSe) windows,” https://www.thorlabs.com/NewGroupPage9.cfm?ObjectGroup_ID=3981.
- [33] Tydex Research and Industrial Optics, “CVD-ZnSe,” http://tydexoptics.com/materials1/for_transmission_optics/cvd_znse/.
- [34] Alfa Aesar, “13241 Zinc selenide, 99.995 % (metals basis),” <http://www.alfa.com/en/catalog/013241/>.
- [35] N. J. Severs, “Freeze-fracture electron microscopy,” *Nat. Protoc.* **2**, 547–576 (2007).
- [36] D. W. Berreman and T. J. Scheffer, “Bragg reflection of light from single-domain cholesteric liquid-crystal films,” *Phys. Rev. Lett.* **25**, 577–581 (1970).
- [37] C. Oldano, P. Allia, and L. Trossi, “Optical properties of anisotropic periodic helical structures,” *J. Phys. (Paris)* **46**, 573–582 (1985).
- [38] I. Abdulhalim, L. Benguigui, and R. Weil, “Selective reflection by helicoidal liquid crystals. Results of an exact calculation using the 4×4 characteristic matrix method,” *J. Phys. (Paris)* **46**, 815–825 (1985).
- [39] V. C. Venugopal and A. Lakhtakia, “Electromagnetic plane-wave response characteristics of non-axially excited slabs of dielectric thin-film helicoidal bianisotropic mediums,” *Proc. R. Soc. Lond. A* **456**, 125–161 (2000).
- [40] M. Schubert and C. M. Herzinger, “Ellipsometry on anisotropic materials: Bragg conditions and phonons in dielectric helical thin films,” *phys. stat. sol. (a)* **188**, 1563–1575 (2001).
- [41] M. Dixit and A. Lakhtakia, “Selection strategy for circular-polarization-sensitive rejection characteristics of electro-optic ambichiral Reusch piles,” *Opt. Commun.* **281**, 4812–4823 (2008).
- [42] H. Takezoe, Y. Ouchi, A. Sugita, M. Hara, A. Fukuda, and E. Kuze, “Experimental observation of the total reflection by a monodomain cholesteric liquid crystal,” *Jap. J. Appl. Phys.* **21**, L390–L392 (1982).
- [43] S. D. Jacobs, K. A. Cerqua, K. L. Marshall, A. Schmid, M. J. Guardalben, and K. J. Skerrett, “Liquid-crystal laser optics: design, fabrication, and performance,” *J. Opt. Soc. Am. B* **6**, 1962–1979 (1988).
- [44] W. D. St. John, W. J. Fritz, Z. J. Lu, and D.-K. Yang, “Bragg reflection from cholesteric liquid crystals,” *Phys. Rev. E* **51**, 1191–1198 (1995).
- [45] I. J. Hodgkinson, Q. Wu, K. E. Thorn, A. Lakhtakia, and M. W. McCall, “Spacerless circular-polarization spectral-hole filters using chiral sculptured thin films: theory and experiment,” *Opt. Commun.* **184**, 57–66 (2000).
- [46] N. J. Podraza, S. M. Pursel, C. Chen, M. W. Horn, and R. W. Collins, “Analysis of the optical properties and structure of serial bi-deposited TiO_2 chiral sculptured thin films using Mueller matrix ellipsometry,” *J. Nanophoton.* **2**, 021930 (2008).

- [47] A. C. van Popta, M. J. Brett, and J. C. Sit, “Double-handed circular Bragg phenomena in polygonal helix thin films,” *J. Appl. Phys.* **98**, 083517 (2005).
- [48] S. Erten, S. E. Swiontek, C. M. Graham, and A. Lakhtakia, “Experimental investigation of circular Bragg phenomenon exhibited by a mirror-backed chiral sculptured thin film,” *J. Nanophoton.* **9**, 090599 (2015).
- [49] G. Ghosh, “Dispersion coefficients for the refractive index and birefringence of calcite and quartz crystals,” *Opt. Commun.* **163**, 95–102 (1999).
- [50] E. U. Condon, “Theories of optical rotatory power,” *Rev. Modern Phys.* **9**, 432–457 (1937).
- [51] T. G. Mackay and A. Lakhtakia, *Electromagnetic Anisotropy and Bianisotropy* (World Scientific, 2010).
- [52] S. Nichols, O. Arteaga, A. Martin, and B. Kahr, “Measurement of transmission and reflection from a thick anisotropic crystal modeled by a sum of incoherent partial waves,” *J. Opt. Soc. Am. A* **32**, 2049–2057 (2015).